




Cooperative response of magnetism and superconductivity in the magnetic superconductor $\text{RbEuFe}_4\text{As}_4$

V. K. Vlasko-Vlasov,¹ U. Welp,¹ A. E. Koshelev,¹ M. Smylie ^{1,2} J.-K. Bao ¹ D. Y. Chung ¹
M. G. Kanatzidis,^{1,3} and W.-K. Kwok¹

¹Materials Sciences Division, Argonne National Laboratory, Argonne, Illinois 60439, USA

²Department of Physics and Astronomy, Hofstra University, Hempstead, New York 11549, USA

³Department of Chemistry, Northwestern University, Evanston, Illinois 60208, USA



(Received 27 November 2019; revised manuscript received 7 February 2020; accepted 12 February 2020; published 11 March 2020)

We present a study of the magnetic-flux evolution in the magnetic superconductor $\text{RbEuFe}_4\text{As}_4$ performed using magneto-optical imaging and magnetization measurements during field cooling and warming and magnetic field cycling at temperatures above and below the magnetic transition point, T_m . The vortex patterns emerging at $T \lesssim T_m$ reveal that the Eu-spin subsystem serves as an internal pump of the magnetic flux while the superconducting critical current controls the delivery of magnetic-flux quanta into the bulk. The interplay of magnetic susceptibility amplifying the magnetic induction and vortex pinning attenuating the magnetic-flux entry results in a field- and temperature-dependent critical state that emulates a paramagnetic Meissner effect. The observed vortex dynamics corresponds to a nontrivial spatial current distribution and yields a self-consistent inhomogeneous enhancement of the sample magnetization.

DOI: [10.1103/PhysRevB.101.104504](https://doi.org/10.1103/PhysRevB.101.104504)

I. INTRODUCTION

Spin symmetry distinguishes the macroscopic quantum coherence in conventional superconductors (SCs) arising from opposite spin Cooper pairs (*s*-wave singlet state) from the spin alignment in ferromagnetic (FM) materials, and often makes these fundamental physical phenomena incompatible. However, coexistence of magnetic order and electron pairing has been discovered in antiferromagnetic and ferromagnetic superconductors such as the rare-earth (RE) molybdenum sulfides (REMo_6S_8) and rhodium borides (RERh_4B_4) with fine scale domain or helical magnetic structures [1–7]. For example, in ErRh_4B_4 and HoMo_6S_8 , the ferromagnetic phase imitates the antiferromagnetic state by forming oppositely magnetized domains smaller than the SC coherence length, which allows, as predicted in [8], FM-SC coexistence at temperatures below the magnetic transition, T_m . Other examples of coexistence were found later in unconventional superconductors, UGe_2 and URhGe , where electrons in the Cooper pairs have the same spin orientation (triplet state) [9,10]. In all these low- T_c SCs the fragile FM-SC coexistence was observed in a very narrow window of parameters (temperature, pressure, and doping).

New interest in the problem of coexistence arose after the discovery of quaternary rare-earth borocarbides ($\text{RENi}_2\text{B}_2\text{C}$) with $T_c \sim 6\text{--}11\text{ K}$ and $T_m \sim 1.5\text{--}11\text{ K}$ [11]. These materials display large variety of magnetic structures, which coexist with superconductivity in a wider temperature range than for previously known ternary compounds. Lately, a robust concurrence of superconductivity and magnetism over a wide temperature range was discovered in the iron-based layered 122 and 1144 iron pnictides, doped EuFe_2As_2 [12–15] and

$(\text{AEu})\text{Fe}_4\text{As}_4$ ($A = \text{Rb}$ or Cs) compounds [16–20]. The advent of these magnetic superconductors with high- T_c (up to $\approx 37\text{ K}$) and $-T_m$ ($\approx 15\text{--}20\text{ K}$) values provides a new platform to investigate the physics of the coexistence of long-range magnetic order and superconductivity. Recent magnetic force microscopy experiments [14,15] found that the Meissner state in $\text{EuFe}_2(\text{As}_{1-x}\text{P}_x)_2$ coexists with small-scale stripe domains with a domain width smaller than the superconducting penetration depth. These domains represent ferromagnetically ordered Eu^{2+} spins that are magnetized perpendicular to the superconducting FeAs planes, which transform into larger domains carrying spontaneously induced vortices at lower temperature.

Previous magnetization [16,17,19] and Mössbauer [21] studies of RbEu-1144 revealed that below T_m the Eu spins order ferromagnetically within the Eu planes, while x-ray and neutron-diffraction studies [22,23] discovered that the spins display helical order along the *c* axis with Eu moments turning by 90° in neighboring Eu layers. Magneto-optical imaging [24] showed that cooling single-crystal samples in an in-plane magnetic field which polarizes the Eu spins towards the field direction at $T \sim T_m$, results in a pronounced enhancement of magnetic flux inside the crystal deep within the superconducting state.

In the present paper, we study this effect in more detail and analyze the magnetic-flux behavior with application of an external field in different directions and at various temperatures. The magnetic-flux distributions visualized by the magneto-optical imaging technique show a remarkable cooperative response of the magnetic and superconducting subsystems. The images depict the paramagnetic Meissner effect, whereby instead of diamagnetic screening a substantial *enhancement*

of the internal magnetic flux is observed upon approaching T_m . This enhancement of the magnetization arises from the entry of Abrikosov vortices nucleated at the sample surface by the strongly increased magnetic susceptibility at T_m . The vortices propagate into the bulk as regulated by vortex pinning, i.e., by the superconducting critical current. This simultaneous self-consistent action of the Eu ions' magnetic moment and the superconducting currents results in a unique nonmonotonic field and temperature response of the studied magnetic superconductor. Below, we present images of the magnetic-flux distributions observed in field cooled, zero-field cooled, and field cycling experiments at different field orientations, and compare them with macroscopic magnetization measurements. We present a model of the self-organized critical state defined by the combined action of superconductivity and magnetism.

II. EXPERIMENT

The studies were carried out on platelet-shaped $\text{RbEuFe}_4\text{As}_4$ single crystals that were grown in a RbAs flux [25]. The crystals had sides of a few hundred micrometers parallel to the ab crystalline plane and were a few tens of micrometers thick.

The macroscopic characterization of the samples has previously been performed using superconducting quantum interference device (SQUID) magnetometry, magnetotransport and specific-heat measurements [19,25,26], which revealed a sharp superconducting transition at $T_c \sim 37$ K ($\Delta T \sim 0.5$ K) and a magnetic ordering transition at $T_m = 15$ K. The superconducting coherence lengths of $\text{RbEuFe}_4\text{As}_4$ are $\xi_c(0) = 0.92$ nm and $\xi_{ab}(0) = 1.4$ nm, as deduced from measurements of the upper critical field, H_{c2} . High-field measurements revealed significant paramagnetic limiting of H_{c2} [27]. The Ginzburg-Landau parameters obtained from the jump in the specific heat and slopes dH_{c2}/dT are $\kappa_c = \lambda_{ab}/\xi_{ab} \sim 67$ and $\kappa_{ab} = [\lambda_c \lambda_{ab} / \xi_c \xi_{ab}]^{1/2} \sim 108$, with penetration depths $\lambda_{ab}(0) = 94$ nm and $\lambda_c(0) = 160$ nm demonstrating that $\text{RbEuFe}_4\text{As}_4$ is clearly a type-II superconductor [19].

The field and temperature dependence of the magnetization in in-plane and out-of-plane applied fields was measured in a SQUID magnetometer. Figure 1 shows representative field cooled cooling, field cooled warming, and zero-field cooled $M(T, H)$ data, as well as in-plane magnetization hysteresis loops. Consistent with reported magnetization and x-ray magnetic scattering results [19,22], already small in-plane fields of the order of a hundred of oersted induce a sizable magnetic moment which has a profound effect on the distribution of magnetic flux as described in detail below. The small in-plane saturation fields confirm that the exchange coupling along the c axis is weak and that the in-plane magnetic anisotropy for the Eu^{2+} ions is small. In contrast, the exchange coupling within the Eu planes and the out-of-plane magnetic anisotropy are large [19,22], inducing quasi-two-dimensional magnetism [26] as is also evidenced by a comparison of the data in Figs. 1(a) and 1(c).

A qualitative distinction between the $M(H)$ loops in Figs. 1(b) and 1(d) is the minimum of magnetization on the descending branch at $H_a || c$, followed by a maximum near $H = 0$. It can be explained by the decreasing contribution to

the total magnetic moment from the magnetic subsystem at lowering H , and the increasing contribution from the critical currents due to the strong field dependence of J_c . These contributions become equal around the minimum of $M(H)$, which confirms a peculiar interplay between the magnetic and SC subsystems. An additional factor causing a sharp shape of the M maximum at $H \rightarrow 0$ should be the entry of negative vortices, often observed in the platelike samples in the perpendicular field, which induces a loop of the increased Meissner current at the plate perimeter [28].

The magnetic-flux distributions were imaged with a magneto-optical indicator (MOI) technique, which enables the visualization and quantitative analysis of the normal component of the magnetic induction, B_z , at the sample surface [29]. The flat ab faces of some of the platelet crystals were glued between two aluminum blocks and their end faces were polished for imaging the flux patterns with field applied along either the ab plane ($H || ab$) or the c axis ($H || c$). The evolution of the flux structure was recorded during both field cooling (FC) and warming (from $T > T_c$ to 5 K and back to $T > T_c$) at different values of H , and during warming following zero-field cooling (ZFC) at different fields applied at 5 K, and in the course of remagnetization (field cycling) at different temperatures.

III. RESULTS AND DISCUSSION

A. Field cooling ($H || ab$) magnetic-flux evolution

Figure 2 illustrates the temperature changes of the spatial flux patterns on the end face of the crystal cooled in the fields of 110, 220, and 330 Oe parallel to the ab plane. The MOI images reveal the flux density, $B_z || H$, in this case perpendicular to the end face. The field was applied at 45 K ($T > T_c$) and cooling was down to 5 K ($T < T_m$). For fields $H < 40$ Oe and at $T < T_m$, the MOI image intensity is only slightly increased (not shown), indicating a small enhancement of the sample magnetization along the field direction. In contrast, for $H_a \gtrsim 50$ Oe, we observe a pronounced inhomogeneous enhancement of B_z at temperatures approaching T_m , induced by certain tilting of helically ordered Eu spins towards H . Such a response highlights the relatively weak interplanar exchange coupling and corresponds to the paramagnetic macroscopic signal near T_m [Fig. 1(a)].

Above T_c , the magneto-optical pictures, referenced by the 42-K image, demonstrate an indistinct homogeneous field distribution throughout the sample (not shown) due to the small magnetic susceptibility of the Eu moments. With decreasing temperatures below T_c , a low-contrast contour line around the sample emerges [Figs. 2(a)–2(c), 27 K]. The contrast is slightly brighter along the sample perimeter indicating an enhancement of B_z near the sample surface. With further cooling, the overall contrast steadily increases [Figs. 2(a)–2(c), 18 K], and at temperatures close to the magnetic transition, T_m , the contrast sharply rises at the sample's left and right narrow ends [Figs. 2(a)–2(c), 15 K].

A further small decrease in temperature enables flux propagation from the ends into the bulk forming bright channels along the midplane of the sample. At larger fields, these channels start forming already slightly above T_m [Fig. 2(c),

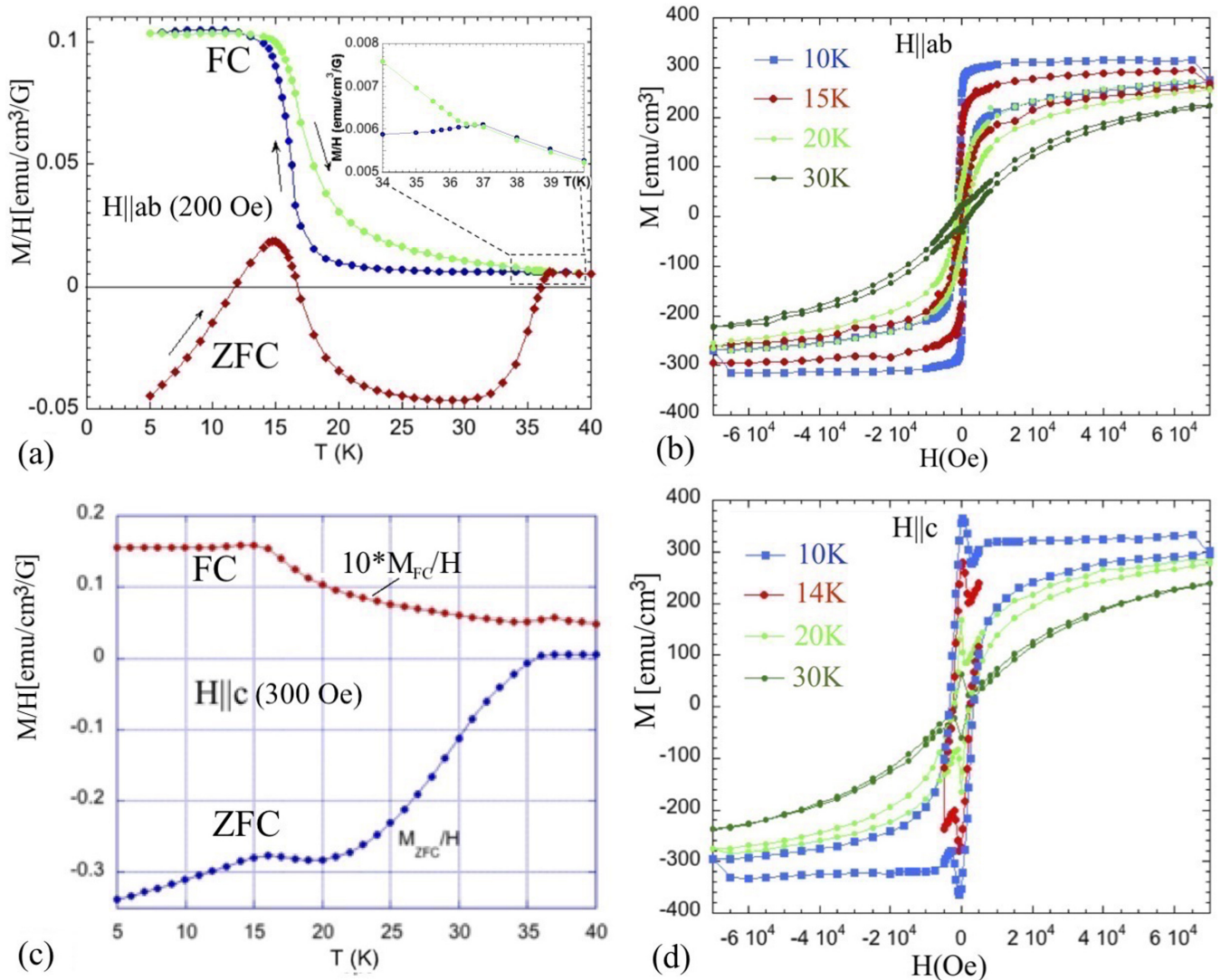


FIG. 1. Magnetization measured under field cooling (FC) and zero-field cooling (ZFC) conditions in (a) $H||ab$ and (c) $H||c$. In (a), FC data on warming and cooling are shown. The inset in (a) displays a close-up of the FC curves near T_c . Note that FC data for $H||c$ in (c) have been multiplied by a factor of 10 for display purposes. (b, d) Magnetization loops at different temperatures for $H||ab$ and $H||c$. In (d) the 14-K loop is presented only for the ± 5000 -Oe range.

18 K]. The flux evolution slows down and saturates at lower temperatures [Figs. 2(a)–2(c), 10 and 5 K] in accordance with leveling of the macroscopic FC $M(T)$ curves in Fig. 1(a). Since the MOI image intensity away from the sample corresponds to H , the increased contrast at temperatures near T_m reveals a strong inhomogeneous enhancement of the magnetic flux ($B > H$) inside the crystal. The behavior is qualitatively the same for all H in Figs. 2(a)–2(c). Quantitatively, with increasing field the concentration of the magnetic flux at the two ends of the crystal becomes stronger and the enhanced flux regions penetrate deeper into the bulk.

Warming the crystal after field cooling to 5 K with the same H , we observe similar flux changes in reverse order [Figs. 2(d)–2(i)], except that the enhanced flux regions survive up to higher temperatures above T_m [Figs. 2(f)–2(h)]. With increasing temperature, the magnetic flux tends to spread from the high- B regions into the neighboring areas and exit the sample, so that B_z decreases towards the edges

[Figs. 2(f)–2(h)]. The escape of flux from the sample is particularly visible along the centerline near the right and left ends where it appears as dark streaks [Fig. 2(g)]. At $T \sim T_c$ the internal B in the sample approaches H and the field contrast mostly disappears [Fig. 2(i)].

Similar FC flux patterns were observed in several samples with different width-to-thickness ratios. In $H||ab$ they consistently demonstrated the enhancement of B_z near the surface at $T \sim T_m$, which was especially strong near narrow ends of the crystals, and the anisotropic flux propagation into the bulk.

Figure 3 shows the variation of the flux density with temperature obtained by averaging the magneto-optical intensity in the area of maximum B near one of the ends of another crystal during the field cooling/warming cycle in $H = 220$ Oe. It confirms the strong enhancement of B_z near T_m , the saturation of B_z at lower T , and the hysteresis of B_z between cooling and warming the sample. These data resemble the macroscopic $M(T)$ curves measured under similar conditions [Fig. 1(a)].

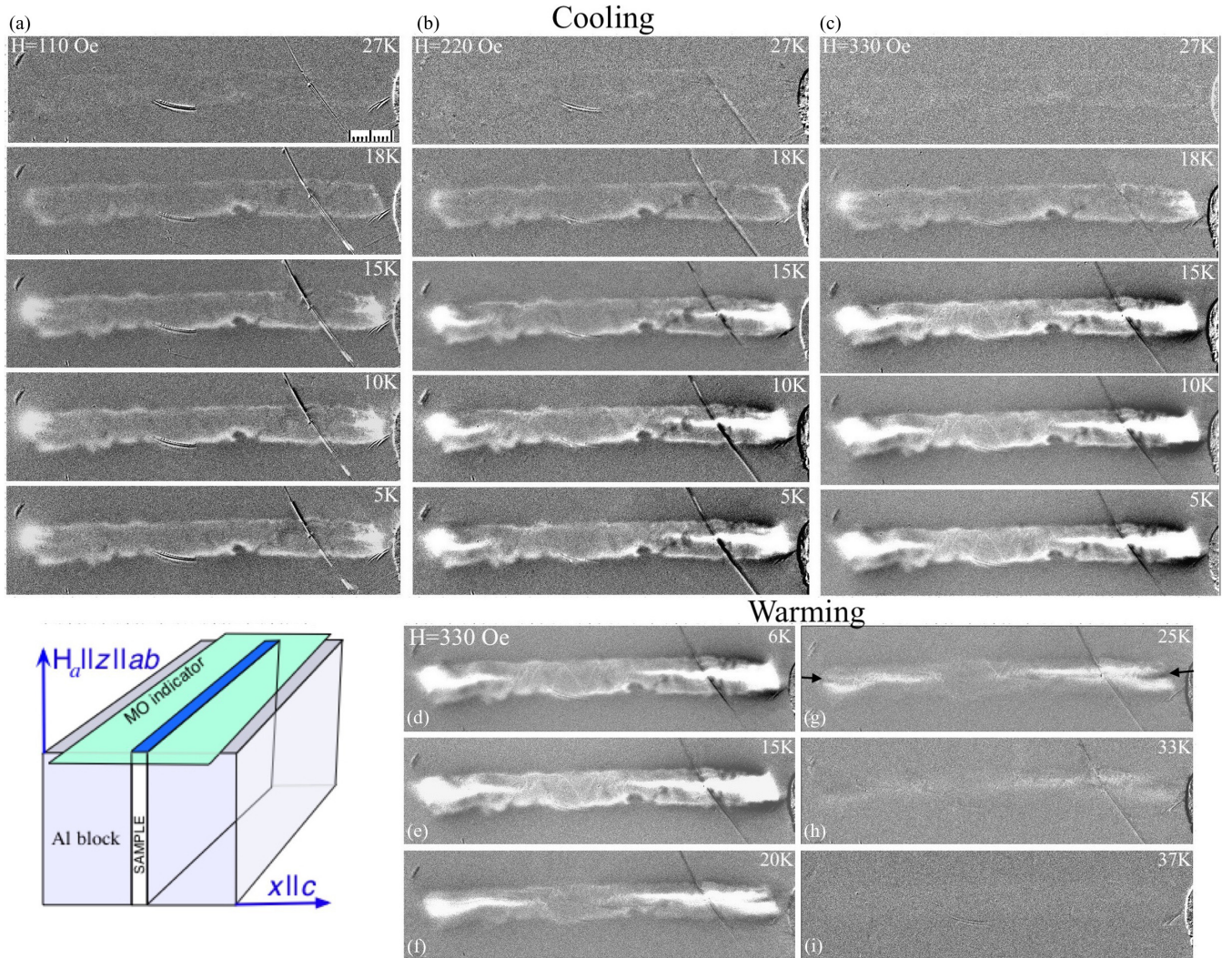


FIG. 2. Comparison of the field patterns emerging during field cooling in magnetic fields of (a) 110, (b) 220, and (c) 330 Oe. Temperatures are indicated in the panels. The intensity of the MOI contrast is a measure of the strength of $B_z || H$. All images are referenced to the 40-K image to decrease the optical noise and to improve the contrast. In (b) and (c), the average intensity of the images is depressed to emphasize changes in the flux penetration. (d-i) evolution of the flux patterns during warming the sample in $H = 330$ Oe after cooling to 5 K in the same field. The experimental geometry sketched on the lower left shows the sample glued between two aluminum blocks and covered with the magneto-optical (MO) indicator. The scale bar in (a) is $100 \mu\text{m}$. The sample width along the z direction is $500 \mu\text{m}$.

However, as the MOI images show, the magnetization distribution at $T \lesssim T_m$ is highly inhomogeneous, which should be considered in the treatment of the macroscopic $M(T, H)$ data.

An interesting feature of the $M(T)$ hysteresis loops measured during the field cooling warming cycle is the kink emerging at $T = T_c$ [Fig. 1(a), inset]. Above T_c , the descending and ascending branches coincide and show a small increase of M with decreasing T , following the paramagnetic response of the Eu spins. At T_c , the cooling branch of the $M(T)$ loop undergoes a downward kink ($dM/dT > 0$) due to the appearance of the diamagnetic Meissner current. However, the warming $M(T)$ branch has an upward kink ($dM/dT < 0$) at $T < T_c$ corresponding to magnetization values that are enhanced above the extrapolated normal-state signal. The latter is due to the vortices accrued during the initial field cooling stage and trapped by paramagnetic critical currents upon warming. In addition, the trapped vortices induce an

enhanced internal field causing a magnetization of the Eu moments above that corresponding to the applied field.

B. Zero-field cooling ($H || ab$) magnetic-flux behavior

In this experiment the sample was cooled in zero magnetic field, followed by the application of $H || ab$ at 5 K. Subsequently, the flux distribution was recorded upon warming the sample in the constant applied field. With the application of H at 5 K, the magnetic field enters from the sample surface as is usually observed in traditional superconductors. Here, similar to the FC case, vortices enter preferentially from the two narrow ends along the a direction and form tapered regions of enhanced B_z extending through the midplane of the sample [Fig. 4(a)]. The flux-free Meissner region is visible as dark areas in the bulk. Upon warming the sample towards T_m at a chosen value of H , the high- B_z regions expand further into

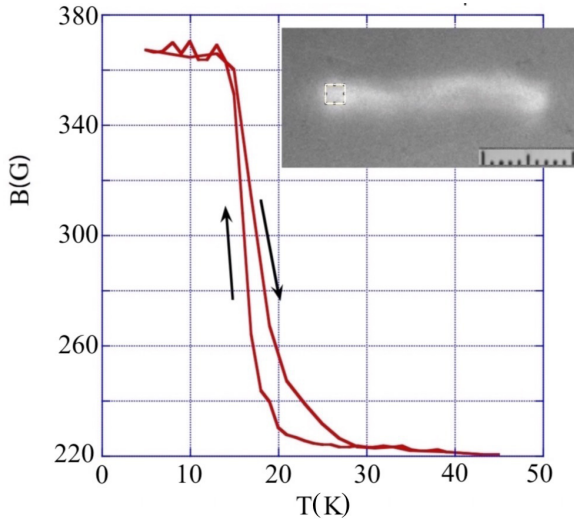


FIG. 3. Temperature dependence of the average induction near one end of the crystal during field cooling or warming in the ab field of 220 Oe. The inset shows a magneto-optical image of the sample with the averaging area marked by the square. The scale bar is $100 \mu\text{m}$. The sample width along the z direction is $300 \mu\text{m}$.

the sample [Figs. 4(b) and 4(c)]. At $T \gtrsim T_m$, B_z begins to decrease, with magnetic flux spreading into the dark Meissner regions and partially exiting the sample [Figs. 4(d)–4(f)]. Up to temperatures close to T_c the contrast over the sample is darker than outside, indicating some degree of diamagnetic screening [Fig. 4(g)]. Finally, at $T \gtrsim T_c$ the field distribution becomes homogeneous [Fig. 4(h)] without any discernable signal from the sample.

C. Field cycling after zero-field cooling ($H||ab$)

In this section we describe flux patterns observed in zero-field cooled samples upon ramping magnetic field up and down at different temperatures. At $T_c > T > T_m$, with increasing $H||ab$, the magnetic-flux penetration follows the typical

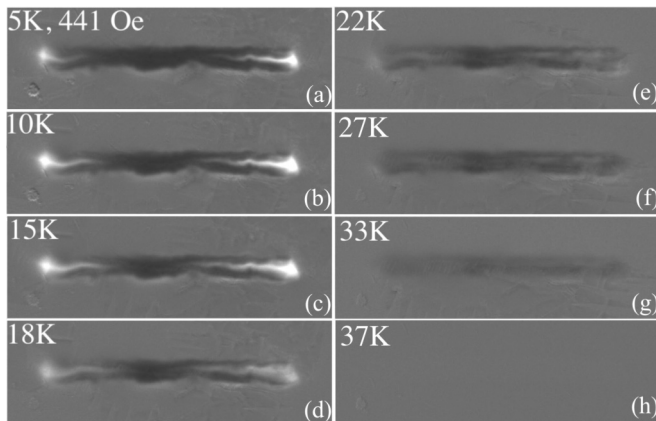


FIG. 4. ZFC flux patterns in the sample during warming in the ab field of 441 Oe applied at 5 K after cooling in $H = 0$. Temperatures are shown in the panels. Pictures are referenced to the 42-K image and a weak contrast above the sample at 37 K is not resolved.

superconducting scenario [Figs. 5(a) and 5(b)]. Namely, small applied fields are screened by the sample and concentrate at the sample boundaries due to diamagnetic Meissner currents (Fig. 5, top panels). At larger H , vortices enter the sample from the surface and disperse inside the bulk due to the Lorentz force induced by the diamagnetic critical currents. The flux density is stronger and penetrates deeper from the narrow left and right ends of the crystal revealing the pinning anisotropy. Similar to the FC and ZFC case, channels of the distinctly enhanced flux density form along the horizontal centerline of the sample. These channels can be due to the weak link for the easy vortex entry created from compositional inhomogeneity that is often observed in flux grown layered samples. However, our energy dispersive spectroscopy analysis did not reveal any compositional changes within the experimental accuracy of 3%. Alternatively, such a flux channel could result from the current instability expected in anisotropic superconductors [30]. With decreasing H , the flux exits towards the sample ends, resulting in areas of reduced B_z along the centerline (dark regions marked by arrows in the bottom panels of Fig. 5).

At $T = T_m$, we observe a strong enhancement of the flux density, with B_z values noticeably exceeding that of the applied field due to flux penetration from the narrow ends of the sample [Fig. 5(c)]. With increasing H the resulting flux patterns become similar to those observed near T_m in the FC case illustrated in Fig. 2. At T well below T_m , the magnetization behavior (not shown) is similar to those at $T = T_m$, albeit the same depth of the flux entry is achieved at much larger H due to the enhancement of vortex pinning at lower temperatures.

D. Imaging the ab surface with field cooling in $H||ab$

Here, the MOI film was placed on top of the wide ab face of the crystal, the magnetic field was applied in the ab plane, and the normal field B_z on the ab surface of the sample was monitored during field cooling. In this geometry, the imaged normal fields reveal tilting of the magnetic-flux lines towards the c axis due to the fields of the superconducting currents and the stray fields of the regions where Eu spins are polarized along H .

A typical set of B_z patterns in one of the samples cooled in $H = 278$ Oe is presented in Fig. 6. Intriguingly, with decreasing temperature, we observe double dark and bright contrast bands at the horizontal sides of the plate that are perpendicular to H [Fig. 6(a)]. At $T \sim T_m$ the dark/bright contrast increases and becomes especially strong near the corners of the crystal [Fig. 6(b)], but then changes only slightly with further cooling. After removing the field at $T = 5$ K, instead of the double dark/bright contrast bands, there is a single bright contrast band at the top and dark contrast band at the bottom, as is generally observed in superconducting plates with in-plane trapped flux. The colors of the described contrasts are inverted when the field direction is changed for its opposite.

The unusual double dark/bright contrast bands at the perimeter of the crystal can be explained with the sketch in Fig. 7. During field cooling, the magnetic flux first enters into the corner regions of the sample as illustrated in Fig. 7(a) by small corner triangles (dark) with dashed-line

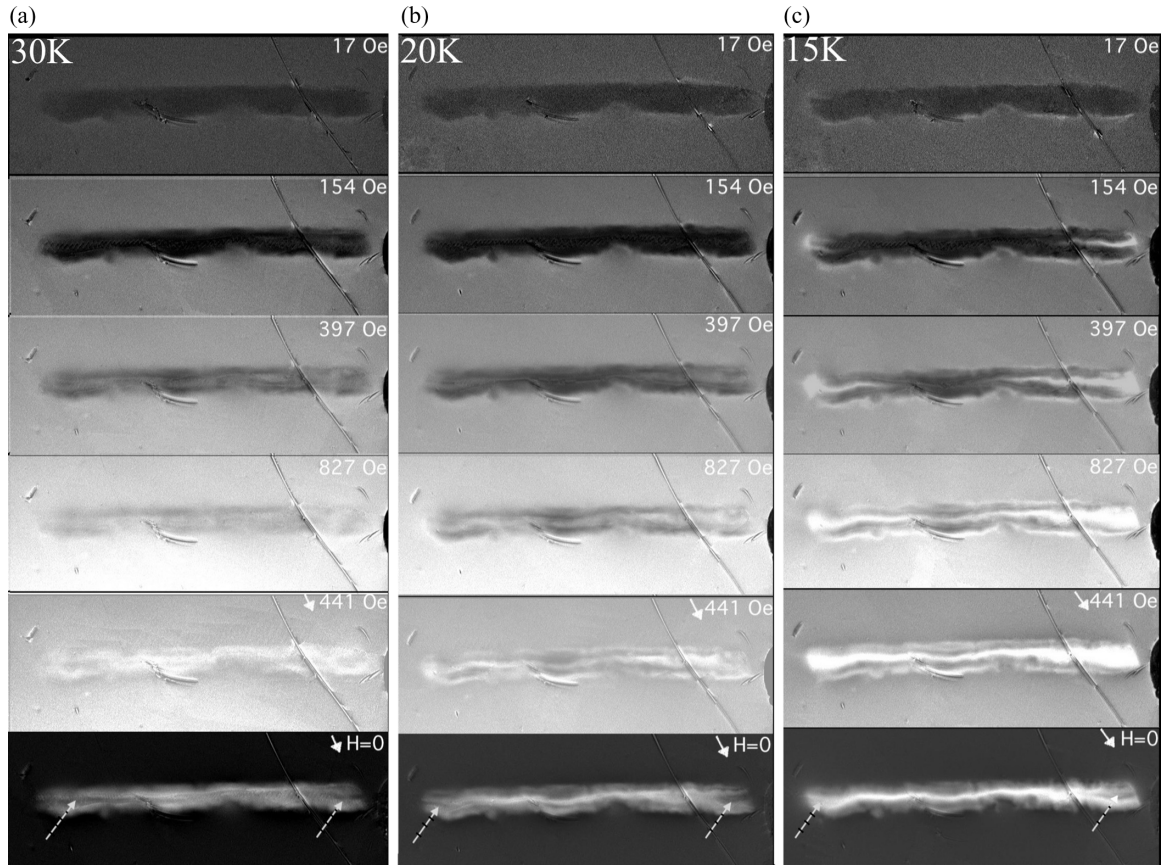


FIG. 5. Comparison of the flux patterns emerging during ramping the field $H||ab$ up and down at (a, b) $T > T_m$ and (c) $T = T_m$. Field values are shown in the panels. Down arrows near the values of H correspond to decreasing applied field. The enhanced flux regions with bright contrast ($B > H$) penetrate into the bulk from the sample perimeter anisotropically with increasing field. At $T < T_m$, patterns similar to those at $T = T_m$ form at larger H [see, e.g., Fig. 4(a)] due to increased pinning at lower temperatures. Long arrows in the bottom panels, at $H = 0$, mark channels of advanced flux exit (darker contrast).

boundaries. Due to the increased magnetic susceptibility, these regions carry enhanced magnetic flux and yield stray fields similar to long magnetic prisms polarized across their length [Pr in Fig. 7(a)]. They have down (blue arrow) and up (red arrow) components of the normal field H_z near the top sample surface. In combination with the effect of diamagnetic supercurrents that tilt the field around the crystal edges [Fig. 7(d)], the resulting field lines wiggle at the edges up and down as shown for the top sample surface in Fig. 7(a). Near T_m , enhanced magnetic flux enters preferentially near the narrow ends, as discussed in the previous sections. These enhanced flux regions are equivalent to the longitudinally polarized magnetic prisms inside the sample [Tr in Fig. 7(b)], which yield additional stray fields shown by blue and red arrows. At $T \sim T_m$ and below, the stray fields of these enhanced flux regions dominate, negating the double contrast bands and resulting in a strong dark or bright contrast at the sample corners (long vertical arrows near the corners in Fig. 7(b) as we observe in the experiment [Fig. 6(b)]. With decreasing H at low T , the superconducting currents change direction and support the field of the penetrated magnetic flux [Fig. 7(c)]. The picture [Fig. 6(c)] then becomes similar to the trapped flux pattern in a nonmagnetic superconductor [Fig. 7(e)] or in an in-plane polarized magnetic plate.

E. Imaging the ab surface with field cycling in $H||c$

Figure 8 illustrates the magnetization process for $H||c$ perpendicular to the ab surface of the crystal at $T \geq T_m$. At these temperatures, similar to nonmagnetic superconducting samples, the flux smoothly penetrates from the edges upon increasing field and then exits towards the edges with decreasing field to zero. At $H = 0$ (after application of $H^{\max} = 827$ Oe), near the edges of the sample, the flux reverses sign (dark contrast in the bottom panels of Fig. 8) due to the stray fields of the trapped vortices. Contrary to the $H||ab$ case, there is no enhanced flux entry at T_m , but rather a more shallow flux penetration than at larger temperatures. Nevertheless, in the vortex occupied areas, the induction is stronger at T_m than at $T > T_m$.

These flux patterns reveal a major role of the bulk critical currents (i.e., vortex pinning) and a marginal contribution of the magnetic subsystem in the magnetic response at moderate $H||c$. Obviously, the Eu spins are easily polarized in the ab plane but require larger polarizing fields in the c direction due to the magnetic anisotropy of $\text{RbEuFe}_4\text{As}_4$. As a result, the superconducting critical currents locked in the ab plane at $H||c$ dominate the magnetic response. Clearly, the individual vortex structure is different for $H||ab$, when the Eu spins turn towards the field partially unwinding the helical structure

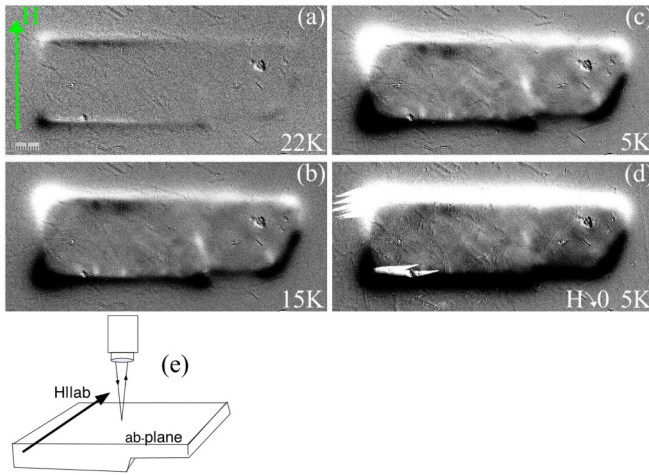


FIG. 6. (a, b) Images of the fields normal to the ab plane during field cooling in the ab field $H = 278$ Oe. In (d) the external field is switched off at 5 K. Dark contrast corresponds to the down component of the field; bright contrast corresponds to the up component. (e) Geometry of the experiment. The right side of the sample has smaller thickness. The contrast in (a) is increased to emphasize the emergence of the double bright/dark B_z image at the sample sides. Scale bar in (a) is $100 \mu\text{m}$. The sample thickness is $80 \mu\text{m}$ in the left and $45 \mu\text{m}$ in the right part, as sketched in (e).

inside the vortex, than for $H||c$, when the Eu moments tilt by a small angle away from the ab plane at the same field values. As a result, the spatial field distribution of the vortex, scaled

by the magnetic permeability of the anisotropic spin system, should depend on the field direction.

In purely FM materials the magnetic anisotropy can be easily determined from $M(H)$ measurements in differently oriented fields. However, in $\text{RbEuFe}_4\text{As}_4$ the tandem action of both magnetic and superconducting subsystems makes the decoupling of their contributions very difficult, allowing only approximate estimates of the magnetic anisotropy constant, K_a . At the same time, the easy-plane character of the anisotropy (ab plane alignment of the Eu spins) clearly follows from the comparison of the $M(H)$ curves for ab and c fields at $T \lesssim T_m$. It is directly confirmed by neutron-scattering experiments [22,23]. Our observations of different flux distributions emerging at $H||ab$ and $H||c$ show that the easy-plane magnetic anisotropy has a strong effect on the vortex structure and dynamics. At the same time, the moderate superconducting anisotropy ($\Gamma = 1.7$ [19]) should have a smaller influence on the vortex motion.

F. Imaging the ab surface with field cooling in $H||c$

The field cooled MOI measurements with $H||c$ confirm the small susceptibility of the Eu spins along the c axis. Flux images obtained under these conditions reveal an enhanced contrast emerging along the edges of the samples which increases upon approaching T_m [Figs. 9(a) and 9(b)]. The strength of this contrast (the flux density) is much weaker than during field cooling in $H||ab$ (Fig. 2), due to the small magnetic contribution arising from slightly tilted Eu^{2+} spins from the ab plane. A similar increased edge field is typical for perpendicularly magnetized FM plates. This field distribution

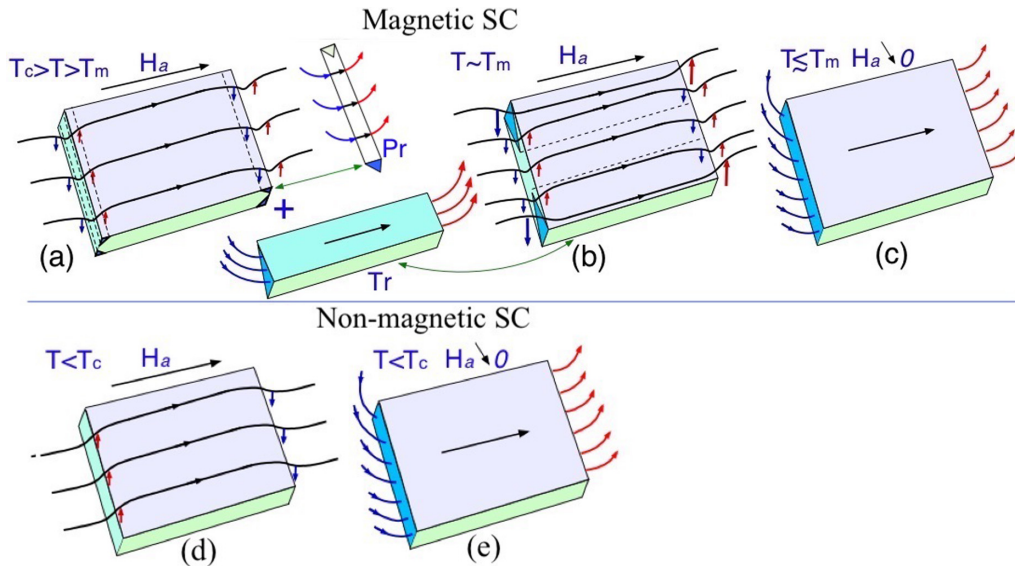


FIG. 7. Field lines near the top surface of the field cooled magnetic superconductor yield double contrast at the sample edges perpendicular to H . A mirror-symmetric picture forms at the bottom surface. Dashed lines in (a) outline narrow corner regions where the flux enters due to the increased magnetic susceptibility upon approaching T_m . Outside the plate, the field lines tilt down into these regions (blue arrows at the left and red arrows at the right sample side). Curvature of the field lines can be approximated by adding stray fields of transversely polarized prisms (Pr) in the corner regions to the fields of the diamagnetic currents sketched in (d). When a strong flux enters from the narrow ends [large “triangular prisms,” Tr, are added to (a)] the stray fields of these high- B regions enhance the normal field components near the plate corners [long vertical blue and red arrows near the plate corners in (b)]. Switching off H_a yields a typical field pattern of a magnetized bar. Bending of field lines in a usual superconducting plate with increasing and decreasing field is shown in (d) and (e).

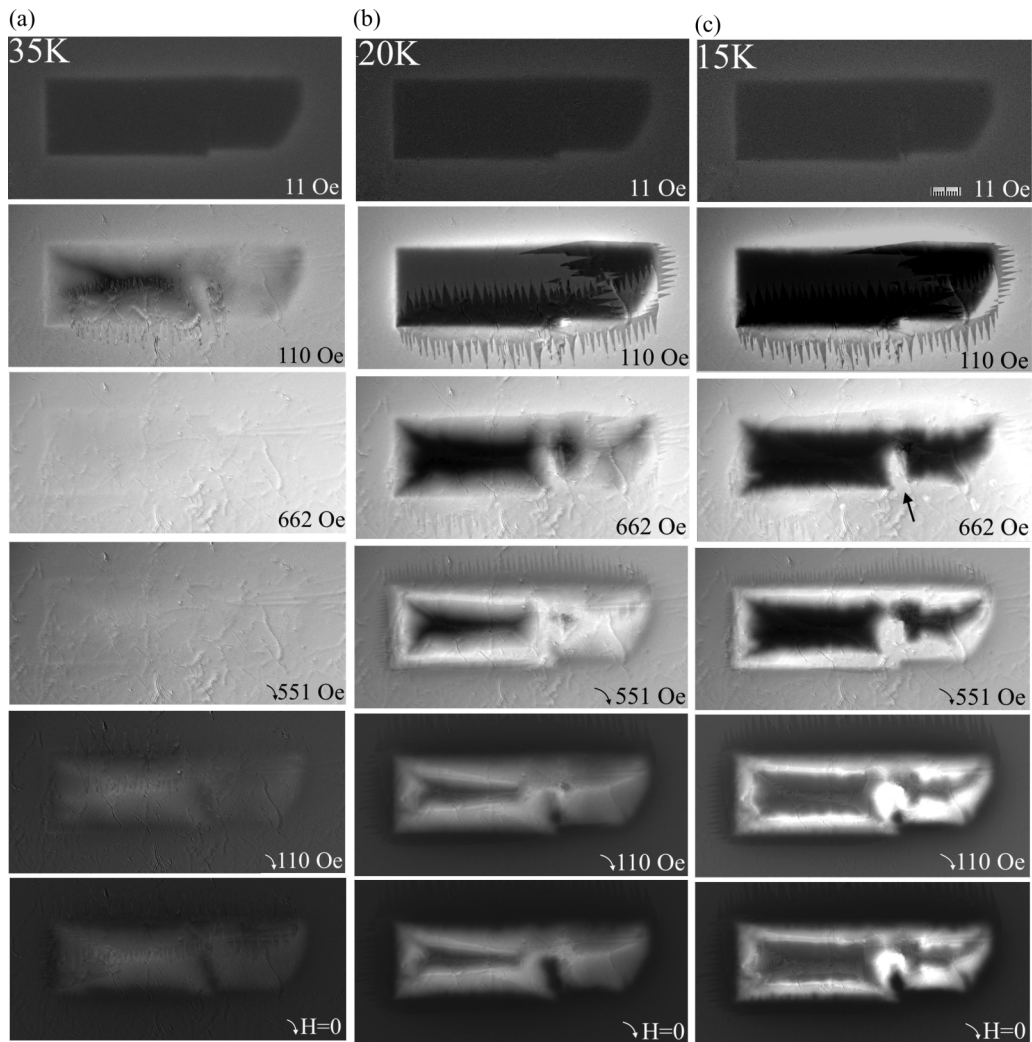


FIG. 8. Flux entry and exit at (a) $T = 35$, (b) 20 , and (c) 15 K in the increasing (top panels) and decreasing (bottom panels with down arrows near H_a values) perpendicular field, $H||c$. Maximum applied field was 827 Oe. Flux patterns for this sample field cooled in $H||ab$ are shown in Fig. 6. The depth of the vortex entry is larger at higher T due to reduced pinning, but the flux patterns are qualitatively similar. Unlike in $H||ab$, there are no peculiarities at T_m (15 K) due to the large magnetic anisotropy restricting the tilt of the Eu^{2+} spins from the ab planes and thus their susceptibility $\chi_{\text{Eu}}||c$. The effect of the superconducting critical currents is dominating and the magnetic subsystem contribution is minor. The scale bar in (c) is $100 \mu\text{m}$. The black arrow in (c) at 662 Oe points to the position of a crack allowing easy flux entry and exit. To the right of the crack the crystal has smaller thickness as sketched in Fig. 6(e).

resembles an electric-field pattern at the perimeter of a charged flat capacitor, where the stray fields are absent in the main capacitor area and appear only near the edges over a width close to the capacitor thickness. However, in $\text{RbEuFe}_4\text{As}_4$ the picture is modified by the entry of vortices supporting the edge field enhancement. The temperature dependence of the maximum edge field, measured from $B_z(x)$ profiles taken across the edge of the sample field cooled in $H = 330$ Oe, is shown in Fig. 9(c). The enhanced edge field increases upon cooling towards T_m and saturates at $T < T_m$. This behavior confirms that the edge contrast is due to the polarization of the Eu ions. The enhancement of the edge field is in sharp contrast to observations in nonmagnetic superconducting plates cooled in perpendicular magnetic fields, from which during field cooling vortices exit near the sample boundaries due to the Meissner effect and the edge fields

become smaller. In our case additional vortices are also generated at the sample perimeter but they remain in a narrow edge rim due to the critical currents which increase upon cooling and restrict the vortex propagation.

G. Short summary of the MOI observations

The main results of our experiments can be recapped as follows. During field cooling of the magnetic superconductor $\text{RbEuFe}_4\text{As}_4$ in fields parallel to the ab plane, a strong enhancement of the induction inside the sample emerges at temperatures near and below the magnetic transition point T_m . In the zero-field cooled case, when the sample is warmed after the application of the field $H||ab$ at low T , the enhanced entry of magnetic flux occurs as T approaches T_m from below. Similarly, when ramping up the field $H||ab$, the advanced

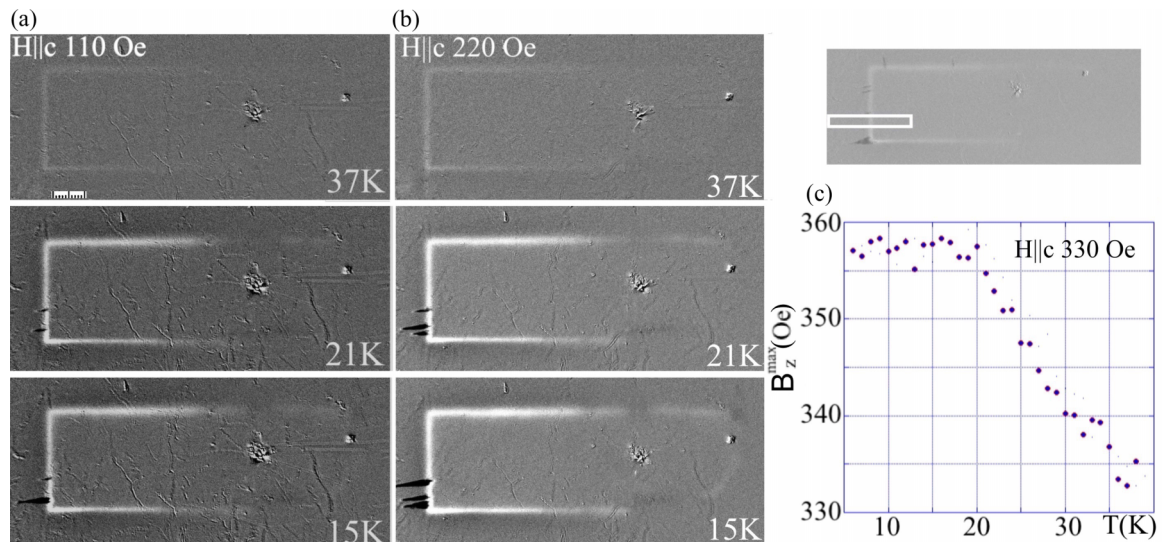


FIG. 9. Flux patterns on the ab surface of the sample during field cooling in $H||c$ at field values of (a) 110 Oe and (b) 220 Oe. The bright contrast is noticeably weaker in the right part of the sample which is thinner as shown in Fig. 6(e). (c) Temperature variations of the maximum edge field, B_z^{\max} , at $H = 330$ Oe. The rectangle in the inset above the plot outlines the strip along which the field profile, $B_z(x)$, was measured. The scale bar shown in (a) is $100 \mu\text{m}$.

penetration of magnetic flux appears at temperatures close to and below T_m . In all these cases the flux enhancement occurs due to the anisotropic entry of additional vortices. Our observations show that in the ordered state the Eu^{2+} -spin system adds to the effect of the applied magnetic field, resulting in an increase of the internal magnetic induction. The additional flux induced by the large magnetic susceptibility (χ_{ab}) of the crystal appears in the shape of the Abrikosov vortices at the sample surface, while their propagation into the bulk is controlled by the superconducting critical currents. Thus, the cooperation of the magnetic and superconducting subsystems creates a peculiar inhomogeneous flux structure in $\text{RbEuFe}_4\text{As}_4$. The contribution of the magnetic subsystem appears distinctly in $H||ab$, where the field drives the Eu spins that are polarized in the ab planes and helically ordered along the c axis, towards the direction of H . These applied fields should be larger than the relatively weak interplanar exchange coupling field responsible for the helical ordering of the ferromagnetic Eu sheets and can be estimated as $H||ab \sim 50\text{--}100$ Oe at $T \lesssim T_m$.

For $H_a||c$, the magnetic susceptibility is much smaller, $\chi_c(T) \ll \chi_{ab}(T)$, due to the easy-plane anisotropy of the Eu spins, and the effect of the magnetic subsystem on the FC, ZFC, and field ramping behavior is much weaker. Here, the magnetization process (at least in moderate fields) is dominated by superconducting currents and is similar to those of nonmagnetic superconductors.

H. Model of the self-induced critical state

Here, we will discuss the peculiar magnetic-flux structure emerging in the vicinity of T_m in terms of the self-induced critical state, which describes a specific induction and current distribution in the magnetic superconductor. Clearly, the observed magnetic-flux enhancement during field cooling of $\text{RbEuFe}_4\text{As}_4$ crystals is in stark contrast with the standard

Meissner effect behavior expected for a conventional superconductor. In a regular SC cooled in a constant magnetic field, vortices exit near the sample surface due to the diamagnetic Meissner current but some remain trapped by the pinning defects in the bulk. The resulting induction profile $B_z(x)$ across the sample should resemble an inverted letter M with minima at the surface and smooth changes of the slope towards the center of the sample, following the cooling history of the sample J_c [Fig. 10(a)].

In contrast, our $\text{RbEuFe}_4\text{As}_4$ crystals show that B_z is enhanced near the edges and decreases towards the interior,

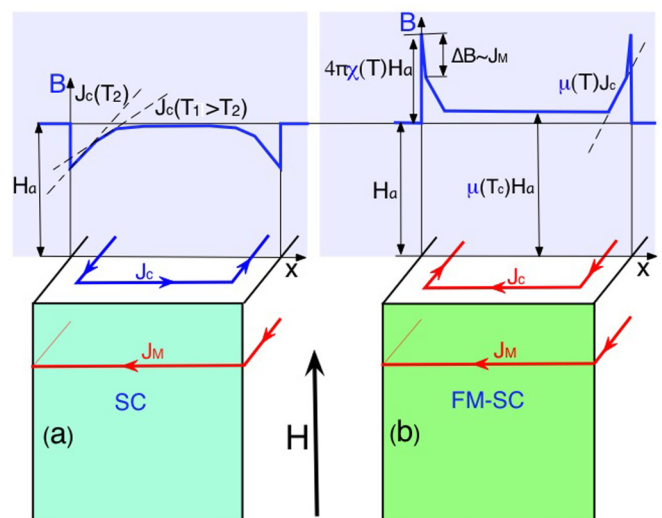


FIG. 10. Induction and current distribution in a field cooled plate (a) of a regular superconductor at $T < T_c$ and (b) in a magnetic superconductor at $T < T_m < T_c$. Changing slope of $B(x)$ proportional to J_c inside the FC SC plate in (a) follows the history of $J_c(T)$ during cooling as shown by dashed lines.

yielding an induction profile opposite to $B_z(x)$ of conventional superconductors. It can be described by the model sketched in Fig. 10(b). At the surface, the magnetic induction is enhanced to a value determined by the susceptibility $\chi_{\text{Eu}}(T)$ of the Eu spins, $B_z = H(1 + 4\pi\chi_{\text{Eu}})$, which is valid in the applied fields that are much smaller than the field of saturation. Away from the surface, B_z drops rapidly by ΔB_M over a distance of the penetration depth or smaller due to the diamagnetic Meissner current $J_M(T)$. This feature is not resolved in our images. Further into the bulk, B_z decays smoothly due to the diamagnetic critical currents $J_c(T)$, while in the middle of the plate the induction remains at the level defined by $\chi_{\text{Eu}}(T_c)$.

For a thin isotropic magnetic superconducting plate of thickness d cooled in a parallel field H_a , and assuming that $\chi_{\text{Eu}}(T) > 0$ varies much faster than $J_c(T)$, a simple estimate of the penetration depth x_c^{FC} for additional vortices generated at the surface yields [24]

$$x_c^{\text{FC}} = \frac{[\mu(T) - \mu(T_c)]H - \Delta B_M}{\frac{4\pi}{c}\mu(T)j_c(T)} \quad (1)$$

Here, $\mu = 1 + 4\pi\chi_{\text{Eu}}$ is the magnetic permeability. In a zero-field cooled sample, when the field is applied at low temperature, the flux entry into the sample interior is delayed by the Meissner currents and the critical currents. In this case, the depth of the Bean profile

$$x_c^{\text{ZFC}} = \frac{H - \frac{\Delta B_M}{\mu(T)}}{\frac{4\pi}{c}j_c(T)} \quad (2)$$

is weakly influenced by the magnetic response. The field of full flux penetration, H_p , at which the flux reaches the center of the plate, $x_c^{\text{ZFC}} = d/2$, can be obtained from (2) as

$$H_p = \frac{2\pi}{c}j_c(T)d + \Delta B_M/\mu(T) \quad (3)$$

For fields below H_p , the sample is in a heterogeneous magnetic state in which a partially polarized helical magnetic structure in the penetrated region coexists with an unperturbed helix in the central parts. Accounting for the fact that the Meissner contribution, ΔB_M , strongly decreases with field, H_p is primarily defined by the SC critical current.

The above simplified model gives a qualitative picture of the flux distribution due to the field enhancement by the magnetic subsystem. A more realistic model should account for the anisotropic critical currents and the nonlocal character of the magnetic susceptibility resulting in an integral magnetic response.

An approach similar to ours was used to explain the magnetization curves in grain aligned powders of $\text{HoBa}_2\text{Cu}_3\text{O}_7$ ($0.14\text{ K} = T_N \ll T \ll T_C = 91\text{ K}$) which contain a large magnetic contribution from the Ho ions [31]. Following [32,33], it was admitted in [31] that due to the effect of magnetic ions the effective penetration depth λ_{eff} should be renormalized by a factor of $\mu^{-1/2}$. As a result, vortices carrying the magnetic-flux quantum Φ_0 become slimmer, with insignificant change in their energy and the first critical field. At the same time, $\mu > 1$ introduces a distinct paramagnetic background to the magnetization curves and increases the induction gradient μ times (without increasing the critical current J_c).

It is interesting to compare the observed FC flux patterns in $\text{RbEuFe}_4\text{As}_4$ with results of the neutron experiments in field cooled crystals of $\text{ErNi}_2\text{B}_2\text{C}$ [34]. The latter revealed a shorter intervortex spacing and decreased intensity of the vortex-lattice diffraction peaks below the transition into the weak-ferromagnetic phase, $T_{\text{WF}} < T_c$. The shorter spacing between vortices corresponds to the enhancement of the flux density and the decreased peak intensity may be related to the increased nonuniformity of the vortex lattice. Our picture of the self-organized FC critical state with locally increased and spatially inhomogeneous vortex distribution explains this behavior.

1. Structure of single vortices in $H_a||ab$

As mentioned above, the main change in the vortex structure due to the magnetic subsystem is the contraction of the vortex diameter $\lambda_{\text{eff}} \sim \lambda/\mu^{1/2}$. A new feature appears at large μ , when the reduction of λ_{eff} may result in the sign inversion of the vortex field, $H_V(r)$, at some distance r from the vortex core. In the London approximation this yields the long-range attraction of vortices and type-I-like superconducting behavior [32,33]. The same conclusion was made in [35] from the analysis of the generalized Ginzburg-Landau functional with material parameters approximating the magnetic superconductor ErRh_4B_4 . It was reported that both SC and FM components are weakened compared to their independent values, λ_{eff} decreases, and $H_V(r)$ reaches a negative minimum at some r . Interestingly, the magnetic order induced by H_V (Fig. 1 in [35]) may expand over scales larger than λ_{eff} , so that already at relatively small vortex density the magnetization distribution should become rather homogeneous, with only weak modulations.

A useful analytical analysis of the Abrikosov vortex structure in the ordered FM/SC state was presented in [36]. This work considers vortices perpendicular to the periodic multilayer of FM and SC components, which simulates the ferromagnetic superconductor with the easy-plane magnetic anisotropy in the normal field. It was shown that the vortex field $H_V(r)$ depends on both the modified effective SC penetration depth $\lambda_{\text{eff}} = \lambda\mu^{-1/2}$ and the characteristic FM length $L = (\alpha/K)^{1/2}$. Here α and K are magnetic exchange and anisotropy constants (as defined in [37]), so that L is a characteristic FM domain-wall width. The vortex field induces a linear tilt of magnetization towards the vortex axis, $M(\parallel H_V) = H/K$, so that $\mu = 1 + 4\pi/K$, which in a certain range of K , α , and λ causes the sign change of H_V at some distance from the vortex core.

In our samples, at $H||ab$, the Eu spins comprising the helical structure twist towards H , which can be approximated by a linear response, $M = H/K_{\text{eff}}$, over relatively wide range of fields (as in non-SC magnetic helical systems [38,39]). Here K_{eff} depicts the magnetic anisotropy, although its origin is the interplanar exchange field which maintains the helical spin structure. Note that in magnetic superconductors the helical spin order is not defined solely by the magnetic subsystem but results from the competition between the FM and SC components, so that even with purely ferromagnetic exchange the magnetic system can transform into the spiral configuration [40,41]. Independently of the nature of the helical spin

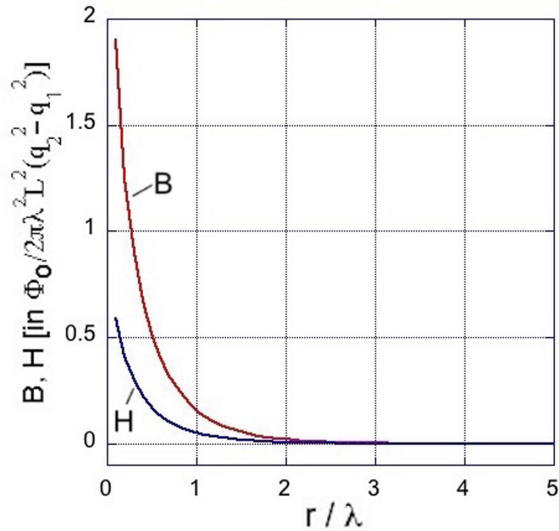


FIG. 11. Single vortex field, $H_V(r)$ (blue), and induction, $B_V(r)$ (red), calculated for $H||ab$ following modified formulas of [36] with magnetic and superconducting parameters estimated for RbEuFe₄As₄ as described in the text.

structure in RbEuFe₄As₄, admitting the linear magnetic response of the Eu spins, we can roughly estimate the value of μ from the slope of the averaged magnetization loops, $M(H)$, at $T \lesssim T_m$ [19]. For $H||ab$ this gives $\mu = 1 + 4\pi/K_{\text{eff}} \sim 3$ at $T \sim 15$ K, so that $K_{\text{eff}} \sim 2\pi$. By adopting the formula for cubic ferromagnets, the exchange constant α can be estimated from the magnetic ordering temperature $T_m \sim 0.7J/k_B$ (here J is the exchange integral and k_B is the Boltzmann constant) and the saturation magnetization of the sample $M_0 = g\mu_B S n/V_c$ ($g = 2$, $S = 7/2$, μ_B is the Bohr magneton, and $n = 4$ is the number of Eu spins per unit-cell volume $V_c = abc$, with lattice parameters $a = b = 3.882$ Å and $c = 13.273$ Å). This yields $\alpha = 2nJS^2/aM_0^2 = 4.4 \times 10^{-12}$ cm², so that $L = (\alpha/K_{\text{eff}})^{1/2} = 8.4$ nm. Neglecting the SC anisotropy and assuming an average penetration depth $\lambda = (\lambda_{ab}\lambda_c)^{1/2} = 122$ nm [19], we estimated the distribution of $H_V(r)$ and $B_V(r)$ following [35], but with modified $\mu_{zz}(q) = 1 + 4\pi/(K + \alpha q^2)$, which appears due to an additional term, $2\pi M^2$, omitted in Eq. (4) of [36]. This changes some formulas of [36] [Eq. (8) for q_2^2 and Eq. (10) for $H_V(r)$], but leaves the equation for $B_V(r)$ intact. As Fig. 11 shows, for the chosen constants of RbEuFe₄As₄ yielding $L \ll \lambda$, neither B_V nor H_V changes sign.

In the field $H||c$ the magnetic permeability is smaller than for $H||ab$ due to the easy-plane anisotropy of the Eu spins, and the effect of the magnetic subsystem on the vortex structure will be weaker. Exact calculations of $B_V(r)$ and $H_V(r)$ accounting for the anisotropy of the SC parameters and accurate estimates of the magnetic constants of RbEuFe₄As₄ will be reported elsewhere [42].

2. Anisotropy of the self-organized critical state

In the cuprate high- T_c superconductors, anisotropic flux dynamics is caused by the layered crystal structure inducing a large anisotropy of the superconducting parameters, $\Gamma = \xi_{ab}/\xi_c$, and affecting the pinning of vortices. In RbEuFe₄As₄,

Γ is small (≈ 1.7), while we see highly anisotropic flux penetration, i.e., large pinning anisotropy, especially at $T \lesssim T_m$. A possible explanation of the large vortex motion anisotropy could be a specific defect structure of RbEuFe₄As₄, as seen, e.g., in a sister material CaKFe₄As₄, where nanometer intergrowth platelets randomly form parallel to the ab plane [43]. However, we suggest that in our crystals the source of the anisotropy could be a self-induced magnetic contribution to pinning. At $H = 0$, the Eu-spin planes order helically with a period of four lattice spacings along the c axis and coexist with superconducting FeAs layers. However, within the vortices oriented along the ab plane, the Eu spins twist towards the field direction. This partially polarized spin state can yield ancillary pair breaking effects in the SC layers (from an average polarization of the conducting electron spins), thus introducing a self-induced vortex pinning. Such a magnetic contribution to pinning in the presence of the layered spin structure and sharp changes of B_V near the vortex center (Fig. 11) could affect the critical current anisotropy.

This conclusion recalls some earlier studies of vortex dynamics in magnetic superconductors. For example, it was predicted in [44] that in magnetic superconductors the local magnetic polarization by the vortex field can substantially increase the viscosity of vortices and retard their motion. Experimentally, a clear effect of magnetic ordering on vortex dynamics was found in single crystals of FM-SC borocarbides such as HoNi₂B₂C [45] and ErNi₂B₂C [46–48]. Here, the rapid increase of the bulk critical current was observed at the transition into the magnetically ordered state, which was referred to as the intrinsic pinning of vortices by the magnetic structure (see also [49]). Interestingly, in superconducting ferromagnets with $T_c \ll T_m$ (Eu_{1.5}Ce_{0.5}RuSr₂Cu₂O₁₀ [50] and UCoGe [51]) a sharp enhancement of the ferromagnetic coercivity was found upon transition into the SC state. This effect of delayed field penetration into the bulk arises due to increased vortex pinning. Unlike in our samples, where entering vortices enhance the bulk magnetization, in the ruthenate and UCoGe, the preexisting M generates spontaneous bulk vortices which are involved in the remagnetization process below T_c . Nevertheless, in both cases, the total magnetic moment of the sample and the spatial flux distribution is defined by the self-organized critical state resulting from the cooperative response of the magnetic and superconducting systems.

In RbEuFe₄As₄, the anisotropy of the self-organized critical state could cause the formation of flux channels observed at $H||ab$ (Figs. 2–5) in the case of a strong field dependence of the critical current causing a positive feedback in the flux penetration. Although the intertwined action of the magnetic and SC subsystem does not allow exact quantitative estimates of the separate magnetic constants and critical currents, it is possible to make a qualitative assessment of the field and temperature dependence of J_c from the half width of the macroscopic magnetization loops. In fact, the $M(H)$ loops display a fast decay of $J_c(H)$ for $H||ab$ (see supplemental information in [24]). Consequently, the enhancement of B_z due to the vortex penetration engaging the internal M should suppress J_c and promote additional vortex entry. In turn, this will initiate a further increase of B and the progressive

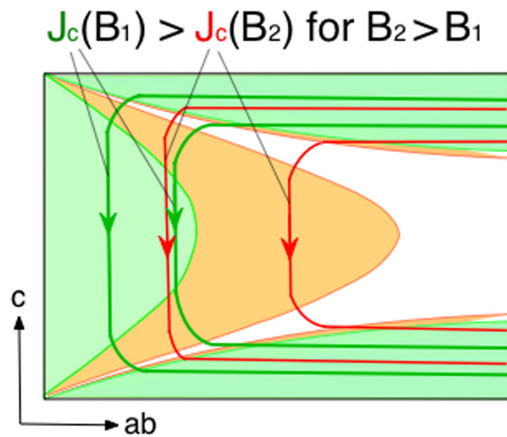


FIG. 12. Progressive extension of the flux occupied region. Increasing B in the shaded areas causes the field suppression of J_c , which allows more vortices to enter and move inside the sample, thus extending the flux front (from green to brown). Distances between the current lines in this sketch illustrate the decreasing J_c . $B_2 > B_1$ in the major extended area.

suppression of J_c , resulting in the extension of the flux occupied regions (see Fig. 12) which can ultimately transform into flux channels.

In the case of $H||c$, the small χ_{Eu} defined by the easy-plane anisotropy of the Eu spins strongly reduces the effect of the magnetic subsystem at low fields even below T_m . As a result, the SC critical currents circulating over a large sample area dominate the magnetization at moderate fields $H||c$ as in the case of nonmagnetic superconductors.

Note that known predictions of various coexistence phases (domain structure, spiral, Meissner, and spontaneous vortices) in magnetic superconductors [33,35,40,41,52–57] are based on the mean-field approximation assuming a *uniform system* state on a scale larger than the period of possible oscillations of the order parameter. In the applied magnetic field the whole system is supposed to uniformly respond to H . Our observations point to the importance of field induced nonuniformity for understanding the magnetic response of FM SCs. The coexisting state in the presence of H is *principally inhomogeneous* independently of the field application sequence. The applied magnetic field does not penetrate inside the entire sample at any $T < T_c$, but has to be delivered into the bulk via the entry of Abrikosov vortices. They will actuate the local alignment of the spins in the crystal interior and induce critical currents supporting gradients of the magnetic induction.

IV. CONCLUSIONS

Our observations of the magnetic-flux patterns under various field directions and field cycling scenarios at temperatures above and below the magnetic transition, T_m , reveal a remarkable cooperative response of the superconducting and magnetic subsystems in single crystals of $RbEuFe_4As_4$. At $T \lesssim T_m$ the large magnetic susceptibility, χ , induces an inhomogeneous enhancement of the internal magnetic flux in the samples. This occurs through the nucleation of Abrikosov vortices at the sample surface and their propagation into the bulk. This propagation is regulated by the superconducting critical currents resulting in an unusual self-organized critical state. Here, the magnetic subsystem acts as an internal stimulant for the magnetic flux while the superconducting subsystem works as a valve controlling the flux propagation into the sample.

Due to the specific structure of the magnetic subsystem, where Eu spins order ferromagnetically and align within the ab planes while maintaining a short-wavelength helical order along the c axis, the magnetic response is strongly anisotropic. For $H||ab$, a relatively small H (a few hundred oersted) twists the Eu spins towards the field direction and noticeably enhances the magnetic subsystem's contribution. However, for $H||c$ a larger field is required to tilt the Eu spins towards H , as it works against the strong anisotropy that keeps the spins in the ab plane. As a result, in moderate $H||c$ (< 2 kOe) the contribution of the magnetic subsystem is small and the magnetic response is dominated by the critical currents, as in regular superconductors.

The main origin of the critical current anisotropy in $RbEuFe_4As_4$ is expected to be the core pinning. The maximum J_c along the ab planes may be due to the layered crystal structure of 1144 and the short coherence length of a few lattice spacings, and possible planar intergrowth defects like in $CaKFe_4As_4$. However, it is not excluded that there is a magnetic component to the pinning anisotropy, when in $H||ab$ the helical arrangement of the Eu spins is untwisted towards a polarized state by the vortex field, thus inducing additional pair breaking.

The intertwined action of the magnetic and superconducting subsystems resulting in the self-organized critical state causes intrinsic inhomogeneity in the spatial distribution of the FM and SC contributions, which should be accounted for in the treatment of the macroscopic $M(H,T)$, neutron, and other measurements in FM SCs.

ACKNOWLEDGMENT

This work was supported by the US Department of Energy, Office of Science, Basic Energy Sciences, Materials Sciences and Engineering Division.

- [1] *Superconductivity in Ternary Compounds II: Superconductivity and Magnetism*, Topics in Current Physics Vol. 34, edited by M. B. Maple and O. Fischer (Springer-Verlag, Berlin, 1982).
- [2] L. N. Bulaevskii, A. I. Buzdin, M. L. Kulić, and S. V. Panjukov, Coexistence of superconductivity and magnetism theoretical predictions and experimental results, *Adv. Phys.* **34**, 175 (1985).

- [3] S. L. Kakani and U. N. Upadhyaya, Magnetic superconductors: A review, *J. Low Temp. Phys.* **70**, 5 (1988).
- [4] O. Peña and M. Sergent, Rare earth based Chevrel phases $REMo_6X_8$: Crystal growth, physical and superconducting properties, *Prog. Sol. St. Chem.* **19**, 165 (1989).

- [5] J. Flouquet and A. Buzdin, Ferromagnetic superconductors, *Phys. World* **15**, 41 (2002).
- [6] M. L. Kulić, Conventional magnetic superconductors: Coexistence of singlet superconductivity and magnetic order, *Compt. Rend. Phys.* **7**, 4 (2006).
- [7] C. T. Wolovlec, B. D. White, and M. B. Maple, Conventional magnetic superconductors, *Physica C* **514**, 113 (2015).
- [8] P. W. Anderson and H. Suhl, Spin alignment in the superconducting state, *Phys. Rev.* **116**, 898 (1959).
- [9] D. Aoki and J. Flouquet, Ferromagnetism and superconductivity in uranium compounds, *J. Phys. Soc. Jpn.* **81**, 011003 (2012).
- [10] D. Aoki, K. Ishida, and J. Flouquet, Review of U-based ferromagnetic superconductors: Comparison between UGe_2 , URhGe , and UCoGe , *J. Phys. Soc. Jpn.* **88**, 022001 (2019).
- [11] C. Mazumdar and R. Nagarajan, Quaternary borocarbides: Relatively high T_c intermetallic superconductors and magnetic superconductors, *Physica C* **514**, 173 (2015).
- [12] A. Pogrebna, T. Mertelj, N. Vujicic, G. Cao, Z. A. Xu, and D. Mihailovic, Coexistence of ferromagnetism and superconductivity in iron based pnictides: A time resolved magneto-optical study, *Sci. Rep.* **5**, 7754 (2015).
- [13] S. Zapf and M. Dressel, Europium-based iron pnictides: A unique laboratory for magnetism, superconductivity and structural effects, *Rep. Prog. Phys.* **80**, 016501 (2017).
- [14] I. S. Veshchunov, L. Ya. Vinnikov, V. S. Stolyarov, N. Zhou, Z. X. Shi, X. F. Xu, S. Yu. Grebenchuk, D. S. Baranov, I. A. Golovchanskiy, S. Pyon, Y. Sun, W. Jiao, G. Cao, T. Tamegai, and A. A. Golubov, Visualization of the magnetic flux structure in phosphorus-doped EuFe_2As_2 single crystals, *JETP Lett.* **105**, 98 (2017).
- [15] V. S. Stolyarov, I. S. Veshchunov, S. Yu. Grebenchuk, D. S. Baranov, I. A. Golovchanskiy, A. G. Shishkin, N. Zhou, Z. Shi, X. Xu, S. Pyon, Y. Sun, W. Jiao, G. H. Cao, L. Ya. Vinnikov, A. A. Golubov, T. Tamegai, A. I. Buzdin, and D. Roditchev, Domain Meissner state and spontaneous vortex-antivortex generation in the ferromagnetic superconductor $\text{EuFe}_2(\text{As}_{0.79}\text{P}_{0.21})_2$, *Sci. Adv.* **4**, eaat1061 (2018).
- [16] K. Kawashima, T. Kinjo, T. Nishio, S. Ishida, H. Fujihisa, Y. Gotoh, K. Kihou, H. Eisaki, Y. Yoshida, and A. Iyo, Superconductivity in Fe-based compound $\text{EuAFe}_4\text{As}_4$ ($A = \text{Rb}$ and Cs), *J. Phys. Soc. Jpn.* **85**, 064710 (2016).
- [17] Y. Liu, Y. B. Liu, Z. T. Tang, H. Jiang, Z. C. Wang, A. Ablimit, W. H. Jiao, Q. Tao, C. M. Feng, Z. A. Xu, and G. H. Cao, Superconductivity and ferromagnetism in hole-doped $\text{RbEuFe}_4\text{As}_4$, *Phys. Rev. B* **93**, 214503 (2016).
- [18] Y. Liu, Y. B. Liu, Y. L. Yu, Q. Tao, C. M. Feng, and G. H. Cao, $\text{RbEu}(\text{Fe}_{1-x}\text{Ni}_x)_4\text{As}_4$: From a ferromagnetic superconductor to a superconducting ferromagnet, *Phys. Rev. B* **96**, 224510 (2017).
- [19] M. P. Smylie, K. Willa, J. K. Bao, K. Ryan, Z. Islam, H. Claus, Y. Simsek, Z. Diao, A. Rydh, A. E. Koshelev, W. K. Kwok, D. Y. Chung, M. G. Kanatzidis, and U. Welp, Anisotropic superconductivity and magnetism in single-crystal $\text{RbEuFe}_4\text{As}_4$, *Phys. Rev. B* **98**, 104503 (2018).
- [20] D. E. Jackson, D. VanGennep, W. Bi, D. Zhang, P. Materne, Y. Liu, G. H. Cao, S. T. Weir, Y. K. Vohra, and J. J. Hamlin, Superconducting and magnetic phase diagram of $\text{RbEuFe}_4\text{As}_4$ and $\text{CsEuFe}_4\text{As}_4$ at high pressure, *Phys. Rev. B* **98**, 014518 (2018).
- [21] M. A. Albedah, F. Nejdassattari, Z. M. Stadnik, Y. Liu, and G. H. Cao, Mossbauer spectroscopy measurements of the 35.5 K superconductor $\text{Rb}_{1-d}\text{EuFe}_4\text{As}_4$, *Phys. Rev. B* **97**, 144426 (2018).
- [22] Z. Islam *et al.* (unpublished).
- [23] K. Iida, Y. Nagai, S. Ishida, M. Ishikado, N. Murai, A. D. Christianson, H. Yoshida, Y. Inamura, H. Nakamura, A. Nakao, K. Munakata, D. Kagerbauer, M. Eisterer, K. Kawashima, Y. Yoshida, H. Eisaki, and A. Iyo, Coexisting spin resonance and long-range magnetic order of Eu in $\text{EuRbFe}_4\text{As}_4$, *Phys. Rev. B* **100**, 014506 (2019).
- [24] V. K. Vlasko-Vlasov, A. E. Koshelev, M. Smylie, J. K. Bao, D. Y. Chung, M. G. Kanatzidis, U. Welp, and W. K. Kwok, Self-induced magnetic flux structure in magnetic superconductor $\text{RbEuFe}_4\text{As}_4$, *Phys. Rev. B* **99**, 134503 (2019).
- [25] J. K. Bao, K. Willa, M. P. Smylie, H. Chen, U. Welp, D. Young Chung, and M. G. Kanatzidis, Single crystal growth and study of the ferromagnetic superconductor $\text{RbEuFe}_4\text{As}_4$, *Cryst. Growth Des.* **18**, 3517 (2018).
- [26] K. Willa, R. Willa, J. K. Bao, A. E. Koshelev, D. Y. Chung, M. G. Kanatzidis, W. K. Kwok, and U. Welp, Strongly fluctuating moments in the high-temperature magnetic superconductor $\text{RbEuFe}_4\text{As}_4$, *Phys. Rev. B* **99**, 180502 (2019).
- [27] M. P. Smylie, A. E. Koshelev, K. Willa, R. Willa, W. K. Kwok, J. K. Bao, D. Y. Chung, M. G. Kanatzidis, J. Singleton, F. F. Balakirev, H. Hebbeker, P. Niraula, E. Bokari, A. Kayani, and U. Welp, Anisotropic upper critical field of pristine and proton-irradiated single crystals of the magnetically ordered superconductor $\text{RbEuFe}_4\text{As}_4$, *Phys. Rev. B* **100**, 054507 (2019).
- [28] V. K. Vlasko-Vlasov, U. Welp, G. W. Crabtree, D. Gunter, V. Kabanov, and V. I. Nikitenko, Meissner holes in superconductors, *Phys. Rev. B* **56**, 5622 (1997).
- [29] V. K. Vlasko-Vlasov, G. W. Crabtree, U. Welp, and V. I. Nikitenko, Magneto-optical studies of magnetization processes in high- T_c superconductors, *NATO ASI Ser. E* **356**, 205 (1999).
- [30] A. Gurevich, Nonlinear flux diffusion in superconductors, *Int. J. Mod. Phys. B* **09**, 1045 (1995).
- [31] O. B. Hyun and I. Hirabayashi, Effects of local moments on the magnetization of $\text{HoBa}_2\text{Cu}_3\text{O}_7$, *Phys. Rev. B* **50**, 16023 (1994).
- [32] M. Tachiki, H. Matsumoto, and H. Umezawa, Mixed state in magnetic superconductors, *Phys. Rev. B* **20**, 1915 (1979).
- [33] H. Matsumoto, R. Teshima, H. Umezawa, and M. Tachiki, Mixed states in ferromagnetic superconductors, *Phys. Rev. B* **27**, 158 (1983).
- [34] H. Kawano-Furukawa, Y. Ishida, F. Yano, R. Nagatomo, A. Noda, T. Nagata, S. Ohira-Kawamura, C. Kobayashi, H. Yoshizawa, K. Littrell, B. L. Winn, N. Furukawa, and H. Takeya, Creation of vortices by ferromagnetic order in $\text{ErNi}_2\text{B}_2\text{C}$, *Physica C* **470**, S716 (2010).
- [35] C. G. Kuper, M. Revzen, and A. Ron, Ferromagnetic Superconductors: A Vortex Phase in Ternary Rare-Earth Compounds, *Phys. Rev. Lett.* **44**, 1545 (1980).
- [36] A. Bespalov, A. S. Melnikov, and A. I. Buzdin, Clustering of vortex matter in superconductor-ferromagnet superlattices, *Eur. Phys. Lett.* **110**, 37003 (2015).
- [37] L. D. Landau and E. M. Lifshitz, *Electrodynamics of Continuous Media* (Elsevier, Amsterdam, 1984).
- [38] A. Hedrpin, P. Meriel, and J. Villain, Antiferromagnetism helicoidal, *J. Phys. Radium* **21**, 67 (1960).

- [39] D. C. Johnston, Unified molecular field theory for collinear and noncollinear Heisenberg antiferromagnets, *Phys. Rev. B* **91**, 064427 (2015); Magnetic structure and magnetization of helical antiferromagnets in high magnetic fields perpendicular to the helix axis at zero temperature, *96*, 104405 (2017).
- [40] L. N. Bulaevskii, A. I. Rusinov, and M. Kucic, Helical ordering of spins in a superconductor, *J. Low Temp. Phys.* **39**, 255 (1980).
- [41] Zh. Devizorova, S. Mironov, and A. Buzdin, Theory of Magnetic Domain Phases in Ferromagnetic Superconductors, *Phys. Rev. Lett.* **122**, 117002 (2019).
- [42] A. E. Koshelev (unpublished).
- [43] S. Ishida, A. Iyo, H. Ogino, H. Eisaki, N. Takeshita, K. Kawashima, K. Yanagisawa, Y. Kobayashi, K. Kimoto, H. Abe, M. Imai, J. Shimoyama, and M. Eistere, Unique defect structure and advantageous vortex pinning properties in superconducting $\text{CaKFe}_4\text{As}_4$, *npj Quant. Mater.* **4**, 27 (2019).
- [44] L. N. Bulaevskii and S. Z. Lin, Polaron-like vortices, dissociation transition, and self-induced pinning in magnetic superconductors, *J. Exp. Theor. Phys.* **117**, 407 (2013).
- [45] C. D. Dewhurst, R. A. Doyle, E. Zeldov, and D. McK. Paul, Interaction between Magnetic Order and the Vortex Lattice in $\text{HoNi}_2\text{B}_2\text{C}$, *Phys. Rev. Lett.* **82**, 827 (1999).
- [46] P. L. Gammel, B. Barber, D. Lopez, A. P. Ramirez, D. J. Bishop, S. L. Budko, and P. C. Canfield, Enhanced Critical Currents of Superconducting $\text{ErNi}_2\text{B}_2\text{C}$ in the Ferromagnetically Ordered State, *Phys. Rev. Lett.* **84**, 2497 (2000).
- [47] C. D. Dewhurst, S. S. James, R. A. Doyle, Y. Paltiel, H. Shtrikman, E. Zeldov, and D. McK. Paul, Vortex pinning by magnetic order in $\text{ErNi}_2\text{B}_2\text{C}$, *Phys. Rev. B* **63**, 060501 (2000).
- [48] S. S. James, C. D. Dewhurst, S. B. Field, D. McK. Paul, Y. Paltiel, H. Shtrikman, E. Zeldov, and A. M. Campbell, Flux pinning mechanisms in $\text{ErNi}_2\text{B}_2\text{C}$, *Phys. Rev. B* **64**, 092512 (2001).
- [49] L. C. Gupta, Superconductivity and magnetism and their interplay in quaternary borocarbides $\text{RNi}_2\text{B}_2\text{C}$, *Adv. Phys.* **55**, 691 (2006).
- [50] E. B. Sonin and I. Felner, Spontaneous vortex phase in a superconducting weak ferromagnet, *Phys. Rev. B* **57**, R14000 (1998).
- [51] K. Deguchi, E. Osaki, S. Ban, N. Tamura, Y. Simura, T. Sakakibara, I. Satoh, and N. K. Sato, Absence of Meissner state and robust ferromagnetism in the superconducting state of UCoGe : Possible evidence of spontaneous vortex state, *J. Phys. Soc. Jpn.* **79**, 083708 (2010).
- [52] E. I. Blount and C. M. Varma, Electromagnetic Effects Near the Superconductor-to-Ferromagnet Transition, *Phys. Rev. Lett.* **42**, 1079 (1979).
- [53] M. Tachiki, H. Matsumoto, T. Koyama, and H. Umezawa, Self-induced vortices in magnetic superconductors, *Solid State Commun.* **34**, 19 (1980).
- [54] L. N. Bulaevskii, A. I. Buzdin, S. V. Panjukov, and M. L. Kucic, Theory of magnetic structure in reentrant magnetic superconductors HoMo_6S_8 and ErRh_4B_4 , *Phys. Rev. B* **28**, 1370 (1983).
- [55] H. S. Greenside, E. I. Blount, and C. M. Varma, Possible Coexisting Superconducting and Magnetic States, *Phys. Rev. Lett.* **46**, 49 (1981).
- [56] O. Sakai, M. Tachiki, H. Matsumoto, and H. Umezawa, Phase diagram in ferromagnetic superconductors, *Solid State Commun.* **39**, 279 (1981).
- [57] T. K. Ng and C. M. Varma, Spontaneous Vortex Phase Discovered? *Phys. Rev. Lett.* **78**, 330 (1997).